submitted to *Geophys. J. Int.*

Melt-band instabilities with two-phase damage

John F. Rudge[1] and David Bercovici[2]

[1] *Bullard Laboratories, Department of Earth Sciences, University of Cambridge, Madingley Road, Cambridge CB3 0EZ, UK. Email: rudge@esc.cam.ac.uk*

[2] *Yale University, Department of Geology & Geophysics, New Haven CT, USA. Email: david.bercovici@yale.edu*

Accepted date. Received date; in original form date

SUMMARY

Deformation experiments on partially molten rocks in simple shear form melt bands at 20° to the shear plane instead of at the expected 45° principal compressive stress direction. These melt bands may play an important role in melt focusing in mid-ocean ridges. Such shallow bands are known to form for two-phase media under shear if strongly non-Newtonian power-law creep is employed for the solid phase, or anisotropy imposed. However laboratory experiments show that shallow bands occur regardless of creep mechanism, even in diffusion creep, which is nominally Newtonian. Here we propose that a couple of forms of two-phase damage allow for shallow melt bands even in diffusion creep.

Key words: Magma migration and fragmentation; Creep and deformation; Rheology: mantle; Mechanics, theory, and modelling; Mid-ocean ridge processes

1 INTRODUCTION

The rheology of partially molten rock is poorly understood, but forms a crucial component of any dynamical model of melt transport in Earth's mantle. The main approach to obtaining a better understanding has been to perform deformation experiments on partially molten rocks in the labo-

ratory (Daines & Kohlstedt 1997; Holtzman et al. 2003; King et al. 2010; Qi et al. 2013). Through a comparison of the results of these laboratory experiments with theory, better models of rheology can be developed. One of the most striking observations of the experiments is that, when a partially molten rock is sheared, localised bands of concentrated melt form at shallow angles ($\sim 20°$) to the shear plane. The development of such melt bands is of great interest in magma dynamics, as they offer a potential mechanism for rapid transport of melt through Earth's mantle (Kohlstedt & Holtzman 2009).

The development of melt bands was first predicted from two-phase theory by Stevenson (1989), who demonstrated that a two-phase medium that is porosity-weakening is unstable to perturbations in porosity, and naturally forms melt-enriched and melt-depleted regions as it deforms. However, it was also predicted that the melt bands should form aligned with the principal compressive stress direction, which for simple shear is at an angle of 45° (not 20°) to the shear plane (Spiegelman 2003). The early models were all based on a Newtonian rheology for the two phases (melt and solid), and Katz et al. (2006) provided a possible explanation for the shallower angle of the bands by invoking a non-Newtonian strain-rate-weakening rheology for the solid phase. This explanation is at first sight appealing, since mantle minerals are known to deform by power-law creep at high temperatures and moderate stresses by the process of dislocation climb. However, there are two important problems with invoking a power-law rheology for the solid phase: First, the power-law exponents required to explain the observed melt band angles are somewhat high ($\mathfrak{n} \sim 4$ to 6), higher than is typical for dislocation creep of olivine ($\mathfrak{n} \sim 3$). Second, and perhaps more importantly, a number of the laboratory experiments have been carried out under grain-size, stress, and temperature conditions for which diffusion creep is dominant, and yet shallow melt bands are still observed.

More recently, another possible explanation has been put forth for the shallow angle of the bands, based on the notion of anisotropy in the effective viscosity tensor, which arises as a result of changes in the distribution of contact area between solid grains (Takei & Holtzman 2009; Butler 2012; Takei & Katz 2013; Katz & Takei 2013). In such models, the resulting melt band angle

depends strongly on the assumed initial anisotropy, which is not well constrained. Here we provide an alternative model, based on isotropic two-phase damage theory (Bercovici et al. 2001; Bercovici & Ricard 2003, 2005, 2012), which can equally well explain the shallow angle bands, even while the solid grains remain in diffusion creep. The next section presents the underlying theory, and is followed by a discussion of an important limiting case in which the two-phase medium acts as a power-law fluid. A linear stability analysis follows, which determines the growth rate and angle of the melt bands. Numerical results are then given for a few demonstrative cases, to illustrate the spectrum of behaviour that is possible.

2 THEORY

We consider a general theory to describe two potential forms of damage. In both cases damage is done to the interface between phases in that deformational work goes toward making more interface and its attendant surface energy by stretching, stirring or rending. In principle damage can either make new interface by opening up new voids, or make more fine-scale or less rough interface by breaking down or distorting existing pores. The void-generating damage, however, simply causes weakened resistance to compaction (i.e., a dynamically reduced effective bulk viscosity) and thus lacks the requisite nonlinear or non-Newtonian effects in the effective shear viscosity to generate shallow melt bands. Thus here we will pursue only the damage that reduces interface roughness.

Interface damage can lead to a few possible rheological effects. The simplest effect is that more interface simply creates more effective slip surfaces between the matrix and very weak melt, and this directly weakens the matrix. A more complicated effect is that more interface creates more blocking surfaces that pin grain growth in the matrix; as the interface roughness is reduced the pinning surfaces are sharpened, which then pin grains to smaller sizes, thereby weakening the matrix as it flows in diffusion creep (Bercovici & Ricard 2012). The theory developed herein will attempt to capture both effects.

2.1 Mass conservation

Conservation of mass in two-phase continuum mechanics dictates a relation for the volume fraction φ_i of phase i, which, assuming both phases are incompressible and there is no mass exchange between phases, leads to

$$\frac{\partial \varphi_i}{\partial t} + \boldsymbol{\nabla} \cdot (\varphi_i \mathbf{v}_i) = 0 \tag{1}$$

where $\mathbf{v}_i$ is the velocity of phase i. Summing these equations and noting that $\sum_i \varphi_i = 1$, we arrive at

$$\boldsymbol{\nabla} \cdot \bar{\mathbf{v}} = 0 \tag{2}$$

where $\bar{\mathbf{v}} = \sum_i \varphi_i \mathbf{v}_i$. We define $\phi \equiv \varphi_1$ as the volume fraction of the minor phase, here the liquid or melt phase. We also define the unsubscripted $\mathbf{v} = \mathbf{v}_2$ as the velocity of the solid or matrix phase, and $\Delta\mathbf{v} = \mathbf{v}_2 - \mathbf{v}_1$ as the phase separation velocity. We can hence recast (1) and (2) as

$$\frac{D\phi}{Dt} = (1-\phi)\boldsymbol{\nabla} \cdot \mathbf{v} \tag{3}$$

and

$$\boldsymbol{\nabla} \cdot (\mathbf{v} - \phi\Delta\mathbf{v}) = 0 \tag{4}$$

where $D/Dt = \partial/\partial t + \mathbf{v} \cdot \boldsymbol{\nabla}$ is the material derivative in the matrix frame of reference.

2.2 Dynamics

2.2.1 Momentum conservation

The conservation of momentum in a creeping two-phase medium with the possibility of grained phases was prescribed by Bercovici & Ricard (2012), which, ignoring gravity becomes

$$0 = -\varphi_i \boldsymbol{\nabla}\Pi_i + \boldsymbol{\nabla} \cdot (\varphi_i \underline{\boldsymbol{\tau}}_i) \pm c\Delta\mathbf{v} + \omega_i\big(\Delta\Pi\boldsymbol{\nabla}\phi + \boldsymbol{\nabla}(\gamma_{\mathrm{I}}\alpha)\big) \tag{5}$$

where the internal pressure on phase i, Π_i, includes the effect of surface tension on the grain boundaries (Ricard & Bercovici 2009; Bercovici & Ricard 2012), $\underline{\boldsymbol{\tau}}_i$ is the deviatoric stress in phase i, c is the coefficient of drag between phases, $\Delta\Pi = \Pi_2 - \Pi_1$, γ_{I} is the surface tension on

the interface between phases, α is the interface density (interface surface area per unit volume), and ω_i is a weighting factor (such that $\sum_i \omega_i = 1$) which accounts for how much surface tension is embedded in one phase relative to the other. The plus sign is chosen for the $\pm c\Delta\mathbf{v}$ term in (5) for phase 1 (the melt) and the minus sign for phase 2 (the matrix).

2.2.2 *Constitutive laws and rheology*

Since phase 1 is a melt we assume $\underline{\boldsymbol{\tau}}_1 \approx \underline{\mathbf{0}}$ and $\omega_1 \approx 0$. The matrix deviatoric stress is denoted as $\underline{\boldsymbol{\tau}} \equiv \underline{\boldsymbol{\tau}}_2$ and given by

$$\underline{\boldsymbol{\tau}} = 2\mu_s \underline{\boldsymbol{e}} \tag{6}$$

where μ_s is the matrix viscosity and

$$\underline{\boldsymbol{e}} \equiv \frac{1}{2}\left(\boldsymbol{\nabla}\mathbf{v} + [\boldsymbol{\nabla}\mathbf{v}]^{\mathrm{t}}\right) - \frac{1}{3}\boldsymbol{\nabla}\cdot\mathbf{v}\underline{\boldsymbol{I}} \tag{7}$$

is the deviatoric strain-rate tensor. In keeping with prior analysis (McKenzie 1984; Katz et al. 2006; Spiegelman 2003) we note that $\eta \equiv (1-\phi)\mu_s$ is an effective shear viscosity for the two-phase medium. We assume a functional form

$$\eta = \eta_0 e^{-b(\phi-\phi_0)}(r/r_0)^n(\mathsf{R}/\mathsf{R}_0)^m = \eta_0\Lambda(\phi, r, \mathsf{R}) \tag{8}$$

where r is the interface roughness or characteristic radius of curvature (see §2.2.3 and Figure 1), and R is the mean grain-size of the solid phase, both being functions of space and time; ϕ_0, r_0 and R_0 are reference values of melt volume fraction, interface roughness and grain-size, hence η_0 is the effective viscosity at this reference state, and thus $\Lambda(\phi_0, r_0, \mathsf{R}_0) = 1$. The dependence on R is typical for diffusion creep in which $m = 2$ for Nabarro-Herring (grain-volume diffusion) creep or $m = 3$ for Coble (grain-boundary diffusion) creep. The dependence on r is an assumed form to capture the decrease in effective viscosity as the interface roughness is reduced to create more slip surfaces with the melt phase. Although it is possible to construct a composite creep rheology allowing for dislocation and diffusion creep (depending on location in grain-size space on a deformation map; see Rozel et al. 2011; Bercovici & Ricard 2012, 2013) we have assumed

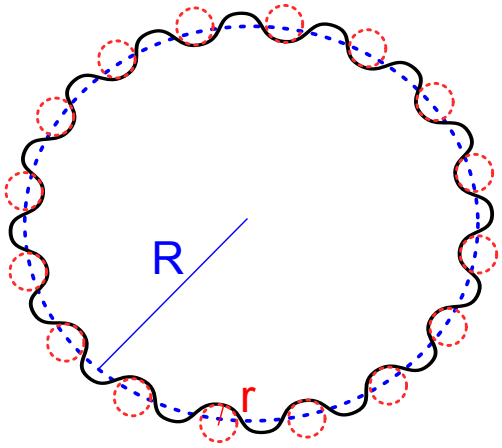

Figure 1. Sketch illustrating the difference between r, the interface roughness or characteristic radius of curvature, and R, the mean grain-size of the solid phase. The black line indicates the boundary between a single solid grain and the melt, the blue dashed line a circle of a radius equal to the mean radius of the grain, and the red dashed lines are circles with a radius equal to the characteristic radius of curvature of the boundary. Figure 2 of Bercovici & Ricard (2012) gives an example of identifying these scales on microscopy images.

that the medium is entirely in diffusion-creep. The main justification for this assumption is that several of the deformation experiments are done with very small grain-sizes and thus are well in diffusion creep. Moreover, the non-Newtonian response of dislocation creep is already known to allow for shallow melt bands, and thus is not new territory. The occurrence of shallow bands in diffusion creep is the more enigmatic phenomenon.

2.2.3 Interface dynamics

The interface density α is a function of both phase volume fraction and interface roughness or radius of curvature r,

$$\alpha = \lambda(\phi)/r \tag{9}$$

where $\lambda(\phi)$ is a prescribed function of ϕ. We will assume a functional form for $\lambda(\phi)$ based on a simple accumulation of spherical pores (Bercovici & Ricard 2012, 2013),

$$\lambda(\phi) = 3\phi(1-\phi). \tag{10}$$

In the absence of void-generating damage, and assuming an inviscid melt, the pressure difference across the interface is simply given by

$$\Delta\Pi = -\frac{\gamma_{\rm I}}{r}\frac{d\lambda}{d\phi} - B(\phi)\frac{D\phi}{Dt} \tag{11}$$

where the second term on the right accounts for viscous resistance to matrix compaction.

2.2.4 Final synthesized force balance equations

Given the assumption of inviscid melt, the force balance equation (5) for the melt (phase 1) becomes Darcy's law

$$\mathbf{0} = -\boldsymbol{\nabla} P + c\Delta\mathbf{v}/\phi \tag{12}$$

where $P \equiv \Pi_1$ is the melt pressure. The interface drag coefficient c is typically written as $c = \phi^2\mu_f/k$ where μ_f is the melt viscosity and k is the matrix permeability (McKenzie 1984). Equation (12) can be substituted into the total conservation of mass statement (4) to yield

$$\boldsymbol{\nabla}\cdot\mathbf{v} - \boldsymbol{\nabla}\cdot\left(\frac{\phi^2}{c}\boldsymbol{\nabla} P\right) = 0. \tag{13}$$

The sum of the two momentum equations in (5) leads to the total conservation of momentum statement

$$\mathbf{0} = -\boldsymbol{\nabla} P + \boldsymbol{\nabla}\left(\zeta\boldsymbol{\nabla}\cdot\mathbf{v}\right) + \boldsymbol{\nabla}\cdot(2\eta\underline{\boldsymbol{e}}) + \gamma_{\rm I}\boldsymbol{\nabla}\mathcal{A} \tag{14}$$

where we define

$$\zeta = (1-\phi)^2 B(\phi) \;\text{ and }\; \mathcal{A} = \frac{(1-\phi)^2}{r}\frac{d}{d\phi}\left(\frac{\lambda}{1-\phi}\right). \tag{15}$$

In what follows we will neglect the $\gamma_{\rm I}\boldsymbol{\nabla}\mathcal{A}$ term in (14), which will be justified by scaling arguments in section 5.1. With the neglect of this term, the momentum equations in (12) and (14) are identical to those of McKenzie (1984), where ζ is the effective bulk viscosity of the two-phase medium.

2.3 Interface evolution and damage

The interface curvature or roughness r evolves both by coarsening (i.e., smoothing of the interface) as well as damage by deformation, distortion and/or rending of the interface. The evolution

equation is given by (see Bercovici & Ricard 2012, 2013, 2014)

$$\frac{Dr}{Dt} = \frac{\lambda G_{\mathrm{I}}}{q r^{q-1}} - \frac{r^2 \mathfrak{f}_{\mathrm{I}}}{\lambda \gamma_{\mathrm{I}}} \Psi \tag{16}$$

where G_I is the interface coarsening coefficient; the exponent q is typically $2 \leq q \leq 4$; $\mathfrak{f}_{\mathrm{I}}$ is the partitioning fraction governing how much deformational work Ψ goes toward creating interface surface energy, and how much (i.e., $1 - \mathfrak{f}_{\mathrm{I}}$) goes to dissipative heating. Damage acts to reduce r, making the interface between the two phases rougher. The deformational work itself is given by

$$\Psi = (1-\phi)\underline{\boldsymbol{\tau}}_2 : \boldsymbol{\nabla}\mathbf{v} = 2\eta \underline{\boldsymbol{e}} : \underline{\boldsymbol{e}}. \tag{17}$$

In the case where weakening occurs only by creation of more slip surfaces through reducing r, then (16) is sufficient to describe the matrix texture, and we can assume $\mathsf{R} = \mathsf{R}_0$ and/or $m = 0$ in (8).

2.4 Grain-growth and pinning

If weakening occurs by grain-size reduction and the dependence of viscosity on grain-size, then we require an evolution equation for R as well. The mean grain-size R of the solid (phase 2) evolves through surface-tension driven coarsening (i.e., normal grain growth). Since the medium is assumed to be in diffusion creep we preclude damage directly to grains, since such grain-reduction requires propagation of dislocations, which only occurs in dislocation creep. However, grain growth is also affected by blocking surfaces imposed by the interface between the two phases (e.g., the contact between olivine and basalt melt), the classic manifestation of which is Zener pinning (Smith 1948). While grain-growth in partial melts possibly obeys Ostwald ripening, experiments in olivine solid with basalt melts indicate coarsening is retarded the same as in any medium with a minor pinning phase (Faul & Scott 2006). Thus it appears, even in such mantle melts, the interface can block grain-boundary migration, and the more curved the interface the more it causes grain-boundary distortion, which can impede and even reverse grain-growth (Bercovici & Ricard 2012).

As shown by Bercovici & Ricard (2012), the evolution equation for the grain-size with pinning

is given by

$$\frac{D\mathsf{R}}{Dt} = \frac{G}{p\mathsf{R}^{p-1}}\left(1 - \mathfrak{c}\phi\frac{\mathsf{R}^2}{r^2}\right) \tag{18}$$

where G is the grain-growth coefficient, and the exponent p is typically 2. The interface blocking of grain growth is given by the Zener pinning factor, i.e., the second factor on the right of (18), where $\mathfrak{c} = 0.87235$ for the log-normal distribution defined by Bercovici & Ricard (2012, 2013). The Zener pinning effect acts to slow down and even reverse growth as r becomes comparable to or smaller than $\sqrt{\mathfrak{c}\phi}\mathsf{R}$.

In the end, damage effectively distorts and sharpens the interface, thus reducing r, which then drives reduction of grain-size R by pinning, even while the medium is in diffusion creep. In this way indirect damage to grains can occur even in the diffusion creep regime, thus leading to a positive self-weakening or shear-localizing feedback. If we account for only this weakening effect and neglect the production of more slip surfaces, then we would set $n = 0$ in (8).

3 THE POWER-LAW LIMIT

Before moving on to a full linear stability analysis of the governing equations it is instructive to consider the effective rheology of the material when the interface roughness and grain-size adjustments are effectively instantaneous relative to the time-scale for deformation. In this limit, we can set the time derivatives on the left hand sides of (16) and (18) to zero, obtaining expressions for the interface curvature r and the grain-size R in terms of the deformational work Ψ as

$$r = \left(\frac{G_{\mathrm{I}}\lambda^2\gamma_{\mathrm{I}}}{q\mathfrak{f}_{\mathrm{I}}\Psi}\right)^{1/(q+1)}, \tag{19}$$

$$R = \frac{r}{\sqrt{\mathfrak{c}\phi}}. \tag{20}$$

Here, damage balances interface coarsening to give an equilibrium interface curvature of (19) which instantaneously pins the grain-size to (20). Substituting the above expressions into (8) yields an effective shear viscosity as

$$\eta(\phi,\Psi) = \eta_0 e^{-b(\phi-\phi_0)}\left(\frac{\phi}{\phi_0}\right)^{-\frac{m}{2}}\left(\frac{\lambda(\phi)}{\lambda(\phi_0)}\right)^{\frac{n+m}{q+1}}\left(\frac{\Psi}{\Psi_0}\right)^{-\frac{n+m}{q+1}}, \tag{21}$$

where for simplicity $\mathfrak{f}_\mathrm{I}/\lambda$ has been assumed constant. In this limit, the material behaves as if it were a power-law fluid, a case which has been studied in detail by Katz et al. (2006). The power-law rheology used by Katz et al. (2006) has the form

$$\eta(\phi,\dot{\epsilon}) = Ae^{\alpha(\phi-\phi_0)}\dot{\varepsilon}^{(1-\mathfrak{n})/\mathfrak{n}} \tag{22}$$

where $\mathfrak{n}$ is the power law exponent, defined so that the strain rate is related to the stress as $\dot{\varepsilon} \propto \sigma^\mathfrak{n}$, in which $\dot{\varepsilon}$ is the second invariant of the deviatoric strain-rate tensor, defined by

$$\dot{\varepsilon} \equiv \left(\tfrac{1}{2}\underline{\boldsymbol{e}}\colon\underline{\boldsymbol{e}}\right)^{1/2} \quad . \tag{23}$$

Equation (22) can be written in terms of the deformational work as

$$\eta(\phi,\Psi) = A'e^{2\mathfrak{n}\alpha(\phi-\phi_0)/(1+\mathfrak{n})}\Psi^{-(\mathfrak{n}-1)/(\mathfrak{n}+1)}. \tag{24}$$

Equating the powers of Ψ in (21) and (24) gives an effective power-law exponent for our rheology as

$$\mathfrak{n} = \frac{q+1+n+m}{q+1-n-m}, \tag{25}$$

and comparison of $\partial\log\eta/\partial\phi$ between (21) and (24) gives an effective porosity weakening exponent as

$$\alpha = -\frac{q+1}{q+1+n+m}\left(b + \frac{m}{2\phi_0} - \frac{n+m}{q+1}\frac{a}{\phi_0}\right), \tag{26}$$

where

$$\frac{a}{\phi_0} = \left.\frac{d\log\lambda}{d\phi}\right|_{\phi=\phi_0}. \tag{27}$$

For the form for $\lambda(\phi)$ proposed in (10), $a \approx 1$.

All the linear stability results of Katz et al. (2006) are applicable to our model in the power-law limit, and (25) and (26) can be used to provide a mapping between their study and ours. In order to generate melt bands at angles other 45°, Katz et al. (2006) found it necessary to invoke large power law exponents, finding an exponent around $\mathfrak{n} = 4$ to 6 to be consistent with the observations. The advantage of the damage theory approach we have taken here is that it provides a justification for large effective power-law exponents even when the grains themselves are deforming by diffusion

creep. Moreover, the damage theory model allows a wider range of behaviour than a simple power-law fluid, behaviour which will be explored later in this manuscript.

4 LINEAR STABILITY ANALYSIS

We now perform a linear stability analysis of the governing equations. We will seek the growth rate of perturbations to a general linear flow

$$\mathbf{v}_0(\mathbf{x}) = \mathbf{x} \cdot \boldsymbol{\nabla}\mathbf{v}_0 \tag{28}$$

where $\mathbf{x}$ is the position vector and $\boldsymbol{\nabla}\mathbf{v}_0$ is a uniform and constant velocity gradient tensor. To satisfy the governing equations, we must have that $\boldsymbol{\nabla} \cdot \mathbf{v}_0 = 0$, so there is no separation of the two phases in the base state. We will define

$$\underline{\mathbf{e}}_0 = \frac{1}{2}\left(\boldsymbol{\nabla}\mathbf{v}_0 + \boldsymbol{\nabla}\mathbf{v}_0^t\right) \tag{29}$$

to be the strain-rate tensor of the base state (also uniform and constant), and

$$\dot{\varepsilon}_0 = \left(\tfrac{1}{2}\underline{\mathbf{e}}_0 \colon \underline{\mathbf{e}}_0\right)^{1/2} \tag{30}$$

to be the second invariant of the base state strain-rate tensor. The base state deformational work is

$$\Psi_0 = 2\eta_0 \underline{\mathbf{e}}_0 \colon \underline{\mathbf{e}}_0 = 4\eta_0 \dot{\varepsilon}_0^2. \tag{31}$$

We consider infinitesimal perturbations to the base state, defining dependent variables as follows:

$$\phi = \phi_0 + \epsilon\phi_1 \tag{32a}$$

$$r = r_0 + \epsilon r_1 \tag{32b}$$

$$\mathsf{R} = \mathsf{R}_0 + \epsilon \mathsf{R}_1 \tag{32c}$$

$$P = P_0 + \epsilon P_1 \tag{32d}$$

$$\mathbf{v} = \mathbf{v}_0(\mathbf{x}) + \epsilon(\boldsymbol{\nabla}\vartheta_1 + \boldsymbol{\nabla} \times \boldsymbol{\psi}_1) \tag{32e}$$

where $\epsilon \ll 1$, ϑ_1 is a scalar potential, $\boldsymbol{\psi}_1$ is a vector potential (where it can be assumed that

$\boldsymbol{\nabla}\cdot\boldsymbol{\psi}_1 = 0$ without loss of generality); all zeroth order variables are uniform and constant except for $\mathbf{v}_0$ which is a function of $\mathbf{x}$, and all first order variables are functions of $\mathbf{x}$ and time t. Substituting (32) into the governing equations (3), (13), (14), (16), and, if necessary, (18) yields equations for the steady state $O(\epsilon^0)$ and for the $O(\epsilon^1)$ perturbations. The $O(\epsilon^0)$ steady-state requires only that

$$r_0 = \left(\frac{G_1\lambda_0^2\gamma_1}{4q\mathfrak{f}_1\eta_0\dot{\varepsilon}_0^2}\right)^{\frac{1}{q+1}} \tag{33}$$

where $\lambda_0 = \lambda(\phi_0)$. In the case of slip-surface weakening we need only specify that R_0 is given; in the case of grain-reduction and pinning, the steady-state solution to (18) is

$$\mathsf{R}_0 = \frac{r_0}{\sqrt{\mathfrak{c}\phi_0}}. \tag{34}$$

For the $O(\epsilon^1)$ equations, mass conservation (3) yields

$$\frac{D_0\phi_1}{Dt} = (1-\phi_0)\mathcal{C}_1 \tag{35}$$

$$\mathcal{C}_1 \equiv \boldsymbol{\nabla}\cdot\mathbf{v}_1 = \nabla^2\vartheta_1 \tag{36}$$

where $\frac{D_0}{Dt} = \frac{\partial}{\partial t} + \mathbf{v}_0\cdot\boldsymbol{\nabla}$. Taking $\boldsymbol{\nabla}\times$ the matrix momentum equation (14) to $O(\epsilon^1)$ leads to

$$\nabla^4\boldsymbol{\psi}_1 = 2\boldsymbol{\nabla}\times(\underline{\boldsymbol{e}}_0\cdot\boldsymbol{\nabla}\Lambda_1) \tag{37}$$

where

$$\Lambda_1 = -b\phi_1 + n\frac{r_1}{r_0} + m\frac{\mathsf{R}_1}{\mathsf{R}_0}. \tag{38}$$

Taking $\boldsymbol{\nabla}\cdot$ of the matrix momentum equation (14) to $O(\epsilon^1)$ and combining with (13) leads to

$$-\left(\zeta_0 + \tfrac{4}{3}\eta_0\right)\nabla^2\mathcal{C}_1 + \frac{c_0}{\phi_0^2}\mathcal{C}_1 = 2\eta_0\underline{\mathbf{e}}_0 : \boldsymbol{\nabla}\boldsymbol{\nabla}\Lambda_1 \tag{39}$$

where $\zeta_0 = \zeta(\phi_0)$. Note that dyadic notation is used throughout this paper (Malvern (1969)).

The evolution equations for r_1 and R_1 become

$$\frac{D_0 r_1}{Dt} = -\frac{G_1\lambda(\phi_0)}{qr_0^{q-1}}\left[(q+1)\frac{r_1}{r_0} + \frac{\Psi_1}{\Psi_0} - \frac{a}{\phi_0}\phi_1\right], \tag{40}$$

$$\frac{D_0\mathsf{R}_1}{Dt} = -\frac{G}{p\mathsf{R}_0^{p-1}}\left[\frac{\phi_1}{\phi_0} + 2\frac{\mathsf{R}_1}{\mathsf{R}_0} - 2\frac{r_1}{r_0}\right], \tag{41}$$

$$\Psi_1 = 2\eta_0\Lambda_1\underline{\mathbf{e}}_0 : \underline{\mathbf{e}}_0 + 4\eta_0\left(\underline{\mathbf{e}}_0 : \boldsymbol{\nabla}\boldsymbol{\nabla}\vartheta_1 + \underline{\mathbf{e}}_0 : \boldsymbol{\nabla}\left(\boldsymbol{\nabla}\times\boldsymbol{\psi}_1\right)\right), \tag{42}$$

where the steady-state $O(\epsilon^0)$ solution (33) and (34) has been used to eliminate factors and for simplicity it has been assumed that $\mathfrak{f}_1/\lambda$ is constant.

4.1 Dimensionless equations

We non-dimensionalize time by $(2\dot{\varepsilon}_0)^{-1}$, r_1 by r_0, R_1 by R_0, and distance by the compaction length

$$\delta = \sqrt{\phi_0^2(\zeta_0 + \tfrac{4}{3}\eta_0)/c_0}. \tag{43}$$

The dimensionless governing equations thus become

$$\frac{D_0\phi_1}{Dt} = (1-\phi_0)\mathcal{C}_1, \tag{44a}$$

$$\nabla^4\boldsymbol{\psi}_1 = 2\boldsymbol{\nabla}\times(\underline{\mathbf{e}}_0\cdot\boldsymbol{\nabla}\Lambda_1), \tag{44b}$$

$$-\nabla^2\mathcal{C}_1 + \mathcal{C}_1 = 2\nu\underline{\mathbf{e}}_0 : \boldsymbol{\nabla}\boldsymbol{\nabla}\Lambda_1, \tag{44c}$$

$$\mathcal{C}_1 = \nabla^2\vartheta_1, \tag{44d}$$

$$\Lambda_1 = -b\phi_1 + nr_1 + m\mathsf{R}_1, \tag{44e}$$

$$\frac{D_0 r_1}{Dt} = -\Gamma_I\left[(q+1)r_1 + \Psi_1 - \frac{a}{\phi_0}\phi_1\right], \tag{44f}$$

$$\frac{D_0\mathsf{R}_1}{Dt} = -\Gamma_g\left[\frac{\phi_1}{\phi_0} + 2\mathsf{R}_1 - 2r_1\right], \tag{44g}$$

$$\Psi_1 = \Lambda_1 + 4\left(\underline{\mathbf{e}}_0 : \boldsymbol{\nabla}\boldsymbol{\nabla}\vartheta_1 + \underline{\mathbf{e}}_0 : \boldsymbol{\nabla}\left(\boldsymbol{\nabla}\times\boldsymbol{\psi}_1\right)\right), \tag{44h}$$

where

$$\nu = \frac{\eta_0}{\zeta_0 + \frac{4}{3}\eta_0}, \tag{45a}$$

$$\Gamma_g = \frac{G}{2p\mathsf{R}_0^p\dot{\varepsilon}_0}, \tag{45b}$$

$$\Gamma_I = \frac{G_1\lambda_0}{2qr_0^q\dot{\varepsilon}_0}. \tag{45c}$$

One of the most important features of the dimensionless governing equations in (44) is that the irrotational component of the flow (described by the scalar potential ϑ_1) is coupled to the solenoidal component of the flow (described by the vector potential $\boldsymbol{\psi}_1$) through the dependence of the viscosity on the interface roughness and grain-size (44e), and their dependence on the vis-

cous dissipation (44f) (and hence both components of the flow (44h)). It is the irrotational part of the flow that drives the growth of the melt bands through compaction (44a): for a Newtonian purely-porosity-weakening rheology the irrotational flow is independent of the solenoidal flow (the right hand side of (44c) would depend only on porosity), and melt bands grow fastest in the principal compressive stress direction. The effect of anisotropy, non-Newtonian power-law rheologies, or the damage rheology we propose here is to couple the solenoidal component to the irrotational component, allowing the dominant melt band growth directions to differ from the principal compressive stress direction.

4.2 Normal mode analysis and dispersion relation

We will seek plane wave solutions of (44) of the form

$$\phi_1(\mathbf{x},t) = \phi_1(t)e^{-i\mathbf{k}(t)\cdot\mathbf{x}}, \tag{46}$$

$$r_1(\mathbf{x},t) = r_1(t)e^{-i\mathbf{k}(t)\cdot\mathbf{x}}, \tag{47}$$

$$\mathsf{R}_1(\mathbf{x},t) = \mathsf{R}_1(t)e^{-i\mathbf{k}(t)\cdot\mathbf{x}}, \tag{48}$$

where $\mathbf{k}(t)$ is the time-varying wave vector of the plane wave. Advection causes the wave vector to stretch and rotate (see discussion in Spiegelman 2003), and its evolution can be described by (Craik & Criminale 1986)

$$\frac{d\mathbf{k}}{dt} = -\boldsymbol{\nabla}\mathbf{v}_0 \cdot \mathbf{k} \tag{49}$$

where $\boldsymbol{\nabla}\mathbf{v}_0$ is the (assumed constant) velocity gradient tensor of the background flow as in (28). The above ODE has solution in terms of a matrix exponential as

$$\mathbf{k}(t) = e^{-t\boldsymbol{\nabla}\mathbf{v}_0} \cdot \mathbf{k}(0) \tag{50}$$

for a given initial wave vector $\mathbf{k}(0)$. From (49) it follows that for any variable $\chi(\mathbf{x},t) = \chi(t)e^{-i\mathbf{k}(t)\cdot\mathbf{x}}$,

$$\frac{D_0\chi}{Dt}(\mathbf{x},t) = \frac{d\chi(t)}{dt}e^{-i\mathbf{k}(t)\cdot\mathbf{x}}. \tag{51}$$

Substituting this relation into (44) yields a set of coupled first order ordinary differential equations for the wave amplitudes

$$\frac{d\phi_1}{dt} = -\nu(1-\phi_0)f(\mathbf{k})\Lambda_1, \tag{52a}$$

$$\frac{dr_1}{dt} = -\Gamma_I\left((q+1)r_1 + (1-2g(\mathbf{k}))\,\Lambda_1 - \frac{a}{\phi_0}\phi_1\right), \tag{52b}$$

$$\frac{d\mathsf{R}_1}{dt} = -\Gamma_g\left(\frac{\phi_1}{\phi_0} + 2\mathsf{R}_1 - 2r_1\right), \tag{52c}$$

$$\Lambda_1 = -b\phi_1 + nr_1 + m\mathsf{R}_1, \tag{52d}$$

$$f(\mathbf{k}) = \frac{2\mathbf{k}\cdot\underline{\mathbf{e}}_0\cdot\mathbf{k}}{1+k^2}, \tag{52e}$$

$$g(\mathbf{k}) = \frac{4\nu(\mathbf{k}\cdot\underline{\mathbf{e}}_0\cdot\mathbf{k})^2}{k^2(1+k^2)} + \frac{4|\mathbf{k}\times\underline{\mathbf{e}}_0\cdot\mathbf{k}|^2}{k^4}. \tag{52f}$$

These can also be cast in matrix form as

$$\frac{d\mathbf{y}(t)}{dt} = \underline{\mathbf{A}}(\mathbf{k}(t))\cdot\mathbf{y}(t) \tag{53}$$

where $\underline{\mathbf{A}}(\mathbf{k})$ is a 3 by 3 matrix which depends on the wave vector $\mathbf{k}$, and $\mathbf{y}(t) = (\phi_1(t), r_1(t), \mathsf{R}_1(t))^t$ is a vector containing the perturbation amplitudes. For any given initial perturbation the above system of ODEs can be integrated along with (49) to give the evolution of the perturbation with time. We are interested in finding the most unstable perturbations, which can be found by considering the eigenvectors and eigenvalues of the matrix $\underline{\mathbf{A}}(\mathbf{k})$. The eigenvalues of $\underline{\mathbf{A}}(\mathbf{k}(t))$ give the instantaneous growth rates for a given wave vector, and in general there are three distinct growth rates corresponding to three distinct eigenmodes.

4.3 Special cases

4.3.1 Power-law limit

When $\Gamma_g \gg 1$ and $\Gamma_I \gg 1$, the system of ODEs reduces to a single ODE for the porosity

$$\begin{aligned}\dot{\phi}_1 &= \nu(1-\phi_0)f(\mathbf{k})\frac{b+\frac{m}{2\phi_0}-\frac{n+m}{q+1}\frac{a}{\phi_0}}{1+\frac{n+m}{q+1}(1-2g(\mathbf{k}))}\phi_1,\\ &= -\frac{\alpha\nu(1-\phi_0)f(\mathbf{k})}{1+\frac{1-\mathfrak{n}}{\mathfrak{n}}g(\mathbf{k})}\phi_1 \end{aligned} \tag{54}$$

using the relationships (25) and (26). As discussed in section 3, in this limit the medium behaves as a power-law fluid with an effective power law exponent $\mathfrak{n}$ given in (25). The expression for the instantaneous growth rate agrees with that of Katz et al. (2006, see supplementary information, S23). Provided $\alpha < 0$ (effective porosity weakening), instability occurs for those wave vectors that have $f(\mathbf{k}) > 0$.

4.3.2 No compaction

If $\nu = 0$ the matrix is uncompactable (infinite effective bulk viscosity) and porosity perturbations do not grow. The evolution equations for r and R are:

$$\dot{r}_1 = -\Gamma_I\left((q+1)r_1 + (1-2g(\mathbf{k}))\,\Lambda_1\right), \tag{55}$$

$$\dot{\mathsf{R}}_1 = -\Gamma_g\left(2\mathsf{R}_1 - 2r_1\right), \tag{56}$$

$$\Lambda_1 = nr_1 + m\mathsf{R}_1. \tag{57}$$

In this case, the trace of the matrix $\underline{\mathbf{A}}$

$$\mathrm{tr}(\underline{\mathbf{A}}) = -\Gamma_I\left(q+1+(1-2g(\mathbf{k}))\,n\right) - 2\Gamma_g, \tag{58}$$

is always negative (since typically $q+1 > n$), while its determinant

$$\det(\underline{\mathbf{A}}) = 2\Gamma_g\Gamma_I\left(q+1+(1-2g(\mathbf{k}))\,(n+m)\right) \tag{59}$$

can have different signs. Provided $q+1 > n+m$, the determinant is always positive and it follows that both eigenvalues have negative real part and there is no instability. However, if $q+1 < n+m$

then for some values of $\mathbf{k}$ the determinant is negative, and there is one positive and one negative eigenvalue, and thus an instability. This corresponds to the case where the effective power law exponent $\mathfrak{n}$ is negative, and the medium is effectively velocity-weakening.

4.3.3 Instantaneous pinning

In the case of instantaneous pinning with $n = 0$ and $\Gamma_g \gg 1$, we use $\mathsf{R}_1 = r_1 - \frac{1}{2}\phi_1/\phi_0$ and the system becomes:

$$\dot{\phi}_1 = -\nu(1-\phi_0)f(\mathbf{k})\Lambda_1, \tag{60a}$$

$$\dot{r}_1 = -\Gamma_I\left((q+1)r_1 + (1-2g(\mathbf{k}))\,\Lambda_1 - \frac{a}{\phi_0}\phi_1\right), \tag{60b}$$

$$\Lambda_1 = -\beta\phi_1 + mr_1, \tag{60c}$$

where $\beta = b + \frac{m}{2\phi_0}$. The determinant of the matrix $\underline{\mathbf{A}}$ is

$$\det(\underline{\mathbf{A}}) = \nu(1-\phi_0)f(\mathbf{k})\Gamma_I\left(\frac{ma}{\phi_0} - \beta(q+1)\right). \tag{61}$$

Since $f(\mathbf{k})$ can be both positive and negative, there is always a range of wave vectors for which the above determinant is negative. For these wave vectors, there is both a positive and a negative eigenvalue, and thus there is always an instability.

4.3.4 All slip-surface weakening

In the case with all slip-surface weakening, $m = 0$ and we neglect the influence of R_1 and the linear system is:

$$\dot{\phi}_1 = -\nu(1-\phi_0)f(\mathbf{k})\Lambda_1, \tag{62a}$$

$$\dot{r}_1 = -\Gamma_I\left((q+1)r_1 + (1-2g(\mathbf{k}))\,\Lambda_1 - \frac{a}{\phi_0}\phi_1\right), \tag{62b}$$

$$\Lambda_1 = -b\phi_1 + nr_1. \tag{62c}$$

Note that this system of equations is identical up to relabelling to that in (60), and thus also always yields an unstable mode.

4.4 Finite strain

The solution of the system of ODEs given in (53) can be written in terms of a matrizant (or propagator matrix) $\underline{\mathbf{P}}(t)$ as

$$\mathbf{y}(t) = \underline{\mathbf{P}}(t) \cdot \mathbf{y}(0) \tag{63}$$

where the matrizant satisfies

$$\frac{d\underline{\mathbf{P}}(t)}{dt} = \underline{\mathbf{A}}(\mathbf{k}(t)) \cdot \underline{\mathbf{P}}(t) \tag{64}$$

and $\underline{\mathbf{P}}(0)$ is the identity matrix. The largest real part of the eigenvalues of the matrizant $\underline{\mathbf{P}}(t)$ gives the largest possible increase in amplitude over a given time period.

5 RESULTS

5.1 Scales and numbers

The dimensionless numbers for the governing equations depend on various experimental parameters. In the shear-deformation experiments of Holtzman et al. (2003), the imposed strain-rate was $\dot{\varepsilon}_0 = 10^{-4}$ s^{-1}, the base state matrix viscosity was approximately $\eta_0 = 10^{12}$ Pa s, and the mean melt volume fraction was $\phi_0 \approx 0.05$. We must have $0 \leq \nu \leq \frac{3}{4}$. Surface tension is typically $\gamma_{\rm I} \approx 1$ Pa m and $\lambda(\phi_0) \approx 3\phi_0$ since $\phi_0 \ll 1$. Interface coarsening is not constrained directly from experiments although it can be inferred from grain-growth experiments in two-phase composites (Bercovici & Ricard 2012). For olivine grain-growth

$$G = 2 \times 10^4 \, \text{s}^{-1} (\mu\text{m})^p e^{-\frac{E_g}{RT}} \tag{65}$$

where $E_g = 200$ kJ/mol is the grain-growth activation energy (Karato 1989; Rozel et al. 2011), T is temperature and $R = 8.3$ J/(mol K) is the gas constant. We can express interface coarsening as $G_{\rm I} = \Phi G \ (\mu\text{m})^{q-p}$ where we use $q = 4$ and $\Phi < 1$ and possibly $\ll 1$, as inferred by Bercovici & Ricard (2012), since diffusion of mass between elements of the minor phase is impeded by the presence of the major phase. For the damage partitioning fraction we assume small values within the range $10^{-4} \leq \mathfrak{f}_{\rm I} \leq 10^{-2}$, which is comparable to that inferred by Rozel et al. (2011) and

Austin & Evans (2007), although these studies were more relevant for damage directly to grains via dynamic recrystallization. The choice of Φ can be estimated by inferring the values necessary to yield $\mathsf{R}_0 = 2\mu$m, which were the typical experimental grain-sizes. At the experimental temperature of $T \approx 1500$ K and using $\mathfrak{f}_{\mathrm{I}} = 10^{-4}$, we obtain $r_0 = 0.4$ μm from (33) and, assuming the mixture is pinned by the minor phase, $\mathsf{R}_0 = 2$ μm from (34) provided $\Phi = \frac{1}{200}$; in this case we would obtain $\Gamma_I = 0.06$ and $\Gamma_g = 1.3$. If we choose $\mathfrak{f}_{\mathrm{I}} = 10^{-2}$ then we would get the same values of r_0 and R_0 provided $\Phi = \frac{1}{2}$; in this case $\Gamma_I = 6$ and Γ_g would remain unchanged.

Alternatively if we use $q = 2$, then we obtain the same results as the case for $\mathfrak{f}_{\mathrm{I}} = 10^{-4}$ and $E_g = 200$ kJ/mol, provided $\Phi = \frac{1}{75}$ (and proportionally larger for $\mathfrak{f}_{\mathrm{I}} = 10^{-2}$). In total these inferred interface coarsening fractions Φ are reasonable and allow for steady values of R_0 consistent with the initial condition of the experiments; i.e., the stability analysis of perturbations to this base state is relevant toward the experiments.

During the analysis we neglected the surface tension term $\gamma_{\mathrm{I}}\boldsymbol{\nabla}\mathcal{A}$ in the force balance of (14). The importance of the surface tension term compared with the viscous terms is determined by a capillary number,

$$\mathrm{Ca} = \frac{\eta_0 \dot{\epsilon}_0 r_0}{\gamma_I}. \tag{66}$$

For the estimates given above, $\mathrm{Ca} = 40$, which is large and justifies the neglect of the surface tension term.

In summary we consider the range of dimensionless numbers given by $0 \leq \nu \leq \frac{3}{4}$, $1 \leq \Gamma_g \leq 100$ and $0.1 \leq \Gamma_I \leq 10$ to be reasonable.

5.2 Instantaneous growth rates for simple shear

We now focus on the specific case of simple shear, which has velocity gradient tensor

$$\nabla \mathbf{v}_0 = \begin{pmatrix} 0 & 1 \\ 0 & 0 \end{pmatrix} \tag{67}$$

in dimensionless form. We write the wave vector as $\mathbf{k} = k(\sin\theta, \cos\theta)$, where θ is the angle of the wavefront to the shear plane, and k is the magnitude of the wave vector. We take the limit of high wavenumber $k \gg 1$, for which (52e) and (52f) become

$$f(\mathbf{k}) \sim \sin 2\theta, \tag{68}$$

$$g(\mathbf{k}) \sim \cos^2 2\theta + \nu \sin^2 2\theta. \tag{69}$$

and the matrix $\underline{\mathbf{A}}(\mathbf{k})$ is purely a function of the wave-vector angle.

Figures 2 - 6 show plots of the eigenvalues of $\underline{\mathbf{A}}(\mathbf{k})$ (the instantaneous growth rates) as a function of the angle of the wavefronts to the shear plane. In each figure the left hand column gives the real part of the eigenvalues, and the right hand column gives the imaginary part. It is only those eigenvalues for which the real part is positive that are unstable, and melt bands are expected to grow fastest at the angles for which the eigenvalues have largest real part.

Figure 2 shows an example of grain-reduction and pinning with $m = 3$ (the grain-size dependence expected in Coble creep) and $n = 0$ (no dependence of the effective shear viscosity on interfacial roughness). The dimensionless rate parameters are chosen as $\Gamma_I = 10$ (interface coarsening) and $\Gamma_g = 100$ (grain growth), towards the high end of the values we think reasonable. Since the matrix $\underline{\mathbf{A}}(\mathbf{k})$ is 3×3 there are three eigenvalues which are shown in the top, middle, and bottom rows in red, green, and blue respectively. The two eigenvalues in the middle and bottom rows always have negative real part and thus do not lead to instability. The eigenvalue in the top row has positive real part for a range of angles, and it is this eigenvalue that gives rise to the melt-banding instability. There are two peaks in the growth rate at 20° and 70° to the shear plane. Although these two peaks have the same instantaneous growth rate, over time it is the melt bands that form at shallow angles to the shear plane which dominate due to rotation by the flow (which will be discussed later in this section). The unstable eigenvalue is well approximated by the solution in the asymptotic limit ($\Gamma_g \gg 1$, $\Gamma_I \gg 1$), which is plotted as the black curve in the top panels. It is in this limit that the medium behaves as a power-law fluid (section 3) with an effective power law exponent $\mathfrak{n} = 4$, and for which the analysis of Katz et al. (2006) holds.

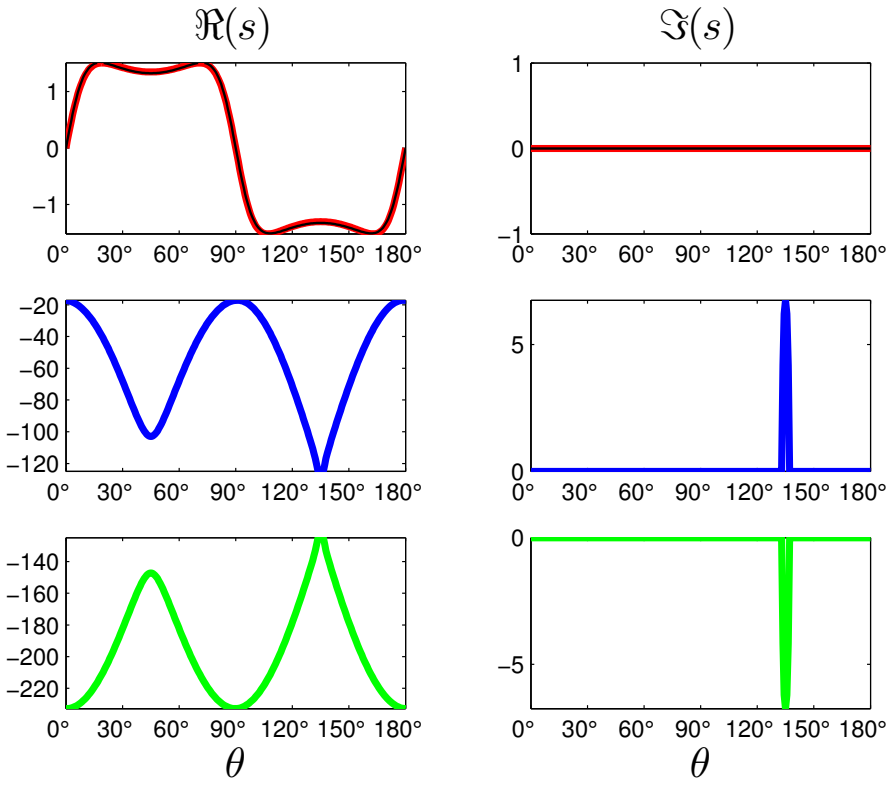

Figure 2. Dispersion curves for three growth rates s (real part in left column, imaginary in right column) against angle to the shear plane θ, for the case with grain reduction and pinning; see (52) with $n = 0$. Parameters are $\Gamma_I = 10$, $\Gamma_g = 100$, $\nu = 0.05$, $m = 3$, $n = 0$, $b = 25$, $q = 4$, and $\phi_0 = 0.05$. The effective power law exponent $\mathfrak{n} = \frac{q+1+n+m}{q+1-n-m} = 4$. The thin black line in the top two panels shows the growth rate expected in the asymptotic power-law limit; see (54).

Figure 3 shows a similar example to Figure 2 where the pinning is instantaneous rather than occurring at a finite rate (i.e. the $\Gamma_g \gg 1$ limit rather than $\Gamma_g = 100$, where the equations reduce to (60)). In this limit there are only two eigenvalues and these are shown in red and blue. The unstable eigenvalue (red) is little different from that in Figure 2, and the stable eigenvalue (blue) is also fairly similar. This is not surprising, as the behaviour for $\Gamma_g = 100$ would be expected to be very close to that of the $\Gamma_g \gg 1$ limit.

Figure 4 shows another example in the same limit of instantaneous pinning as seen in Figure 3 except the rate of interface coarsening has been reduced so that $\Gamma_I = 1$, and the medium is more compactable (a reduced effective bulk viscosity) with $\nu = 1/3$ rather than $\nu = 0.05$ as used in the previous two figures. The asymptotic power-law growth rate is linear in ν (see (54)), so a

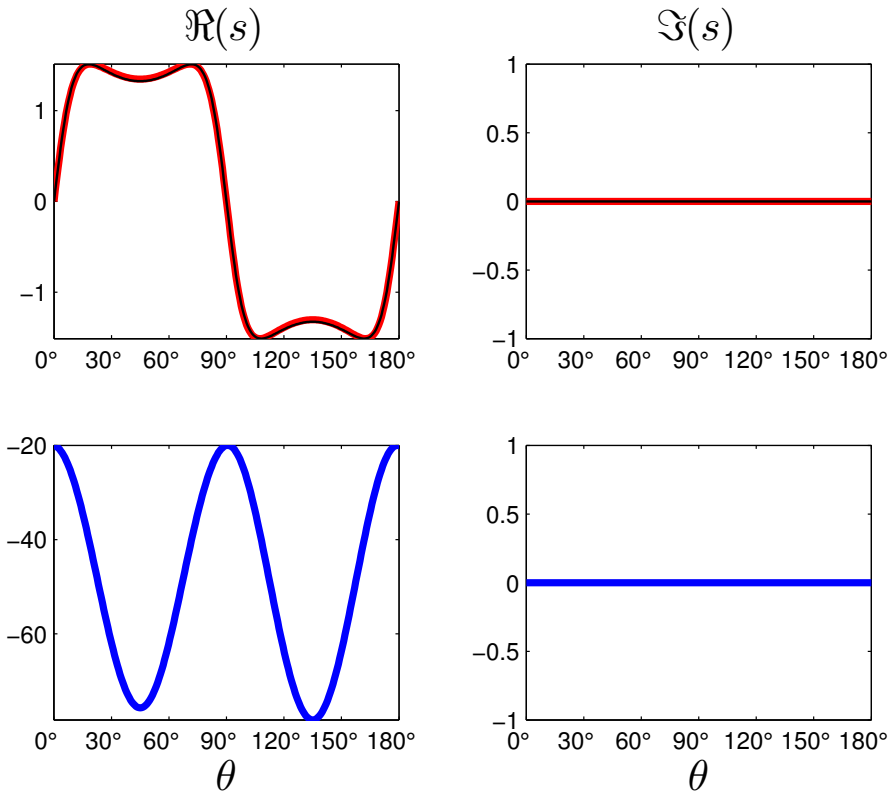

Figure 3. Dispersion curves for two growth rates s for the case of grain-reduction and instantaneous pinning in which $\Gamma_g \gg 1$; see (60). Parameters are $\Gamma_I = 10$, $\nu = 0.05$, $m = 3$, $n = 0$, $b = 25$, $q = 4$, $\phi_0 = 0.05$. The effective power law exponent $\mathfrak{n} = 4$.

change in ν from 0.05 to 1/3 leads to a roughly 7-fold increase in amplitude. However, in this parameter regime the approximation of the power-law limit is not appropriate, and there is a clear difference between the eigenvalue in red and the black curve showing the asymptotic power-law limit in Figure 4. In this particular regime the instability grows fastest at an angle of 45° to the shear plane and thus this parameter regime is not appropriate for explaining the low angle bands seen in experiments.

Figure 5 presents an example with the same parameters as Figure 2 except that $n = 2$ rather than $n = 0$ – this represents a case with *both* slip-surface weakening *and* grain reduction and pinning. In the limit of instantaneous pinning and interface coarsening these parameters would give a power-law fluid with an infinite power-law exponent, the plasticity limit (black curve). In this limit there is an infinite growth rate at 0° and 90° to the shear plane. With finite rates of pinning

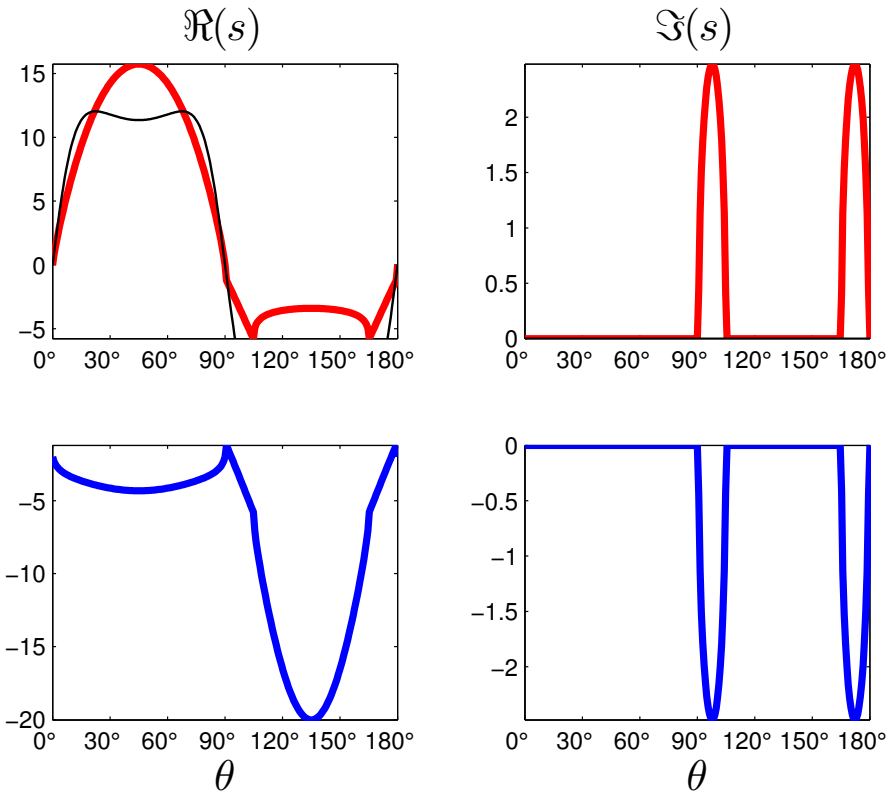

Figure 4. Dispersion curves for two growth rates s for the case of grain-reduction and instantaneous pinning as in Figure 3, with parameters changed so that $\Gamma_I = 1$ and $\nu = 1/3$.

and interface coarsening, the unstable mode has a finite maximum growth rate, and for the example shown in Figure 5 there is a peak at a very shallow angle to the shear plane, at $\sim 6°$.

Figure 6 shows an example with the same parameters as Figure 5 except that $n = 3$ rather than $n = 2$. With these parameters $n + m > q + 1$ and this leads to a medium which is unstable even in the absence of compaction (section 4.3.2). The effective power law exponent becomes negative $\mathfrak{n} = -11$, and the approximation of the medium as a power-law fluid breaks down. A peak in the growth-rate in Figure 6 occurs almost parallel to the shear plane, at $\sim 1°$.

5.3 Growth rate for finite strain

The instantaneous growth rates calculated in the previous section are useful for determining at what angle melt bands are likely to form. However, over time the melt bands rotate in the simple shear flow, moving out of the orientation of maximum growth (Spiegelman 2003). It is the rotation

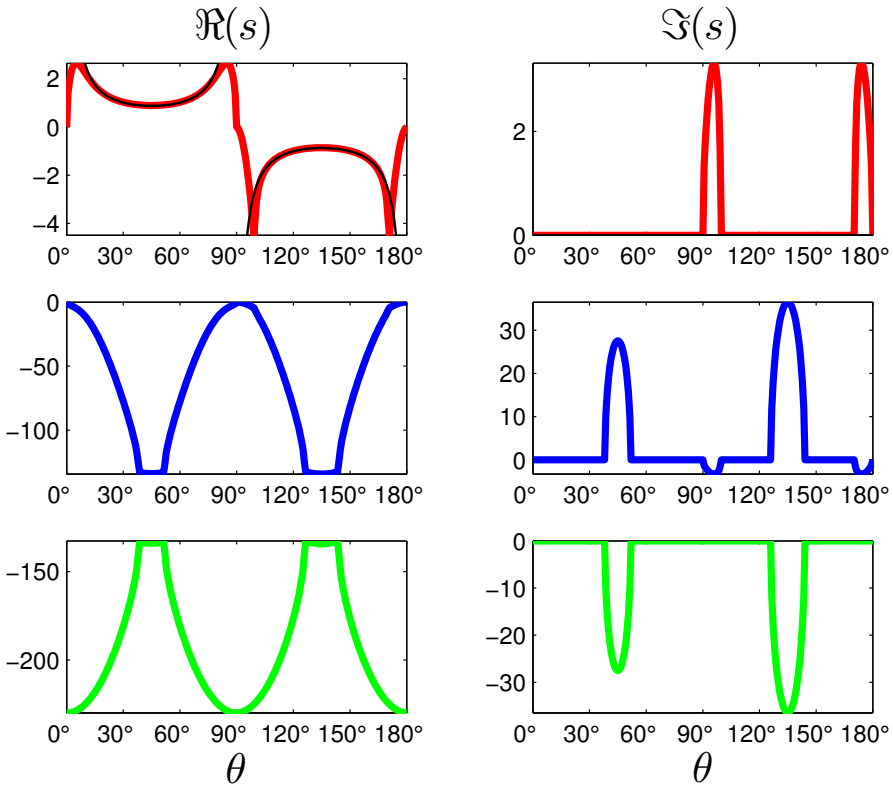

Figure 5. Dispersion curves for three growth rates s for the case with *both* slip-surface weakening *and* grain reduction and pinning; see (52). Parameters are $\Gamma_I = 10$, $\Gamma_g = 100$, $\nu = 0.05$, $m = 3$, $n = 2$, $b = 25$, $q = 4$, and $\phi_0 = 0.05$. With these parameters, this case represents the plasticity limit in which the effective rheological power-law exponent $\mathfrak{n} = \infty$.

by the flow that means that bands at shallow angles are dominant over those at steeper angles, even though both have the same instantaneous growth rate.

As discussed in section 4.4, the growth of perturbations over finite time can be calculated from the eigenvalues of the matrizant $\underline{\mathbf{P}}(t)$. An example of this is shown in Figure 7, where the blue curve shows the relative amplitude of the largest growing perturbation after a finite strain of $\gamma = 1.0$ for the parameters in Figure 3 (grain-reduction and pinning). This blue curve was calculated from a joint integration of (64) and (49) for a range of initial wave vector angles. Due to the rotation by the flow the wave vector angle changes over time, and the x-axis of Figure 7 gives the angle of the wave-front after straining, corresponding to $\mathbf{k}(1.0)$. The y-axis give the relative amplitude of the largest growing perturbation, which corresponds to the eigenvalue of the matrizant $\underline{\mathbf{P}}(1.0)$

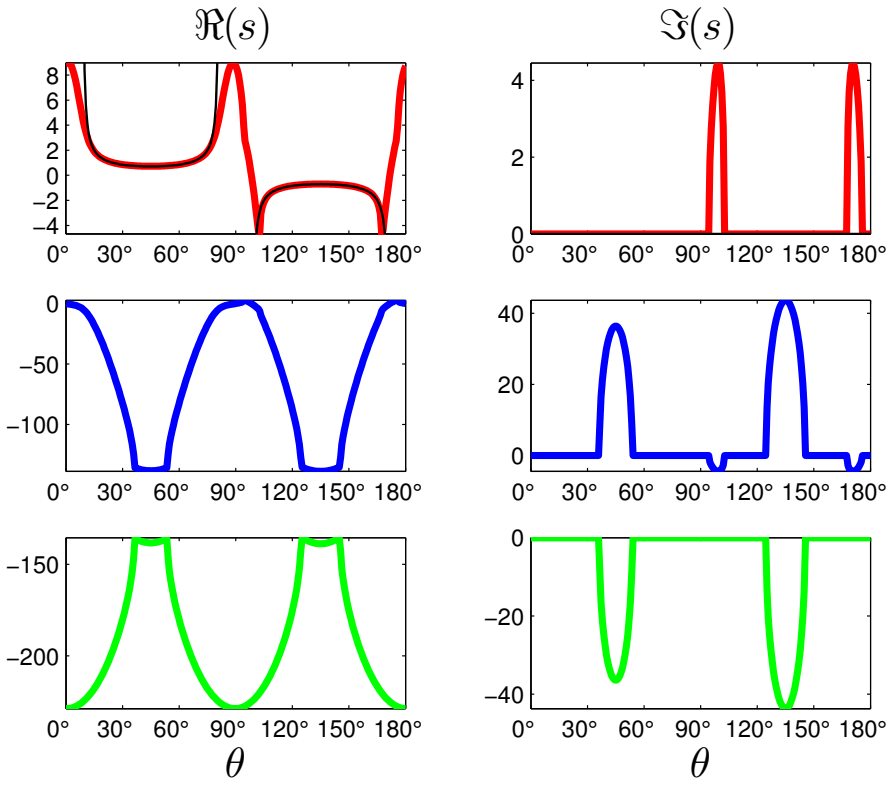

Figure 6. Dispersion curves for three growth rates s with the same parameters as in Figure 5 except for $n = 3$. This case represents the velocity weakening limit in which the effective rheological power-law exponent $\mathfrak{n} = -11 < 0$.

with largest real part. Also shown in the black curve in Figure 7 is the expected amplitude in the power-law limit, which as expected provides a good match. The asymmetry that develops between the shallow and steep bands is clear, with the maximum amplitude occurring for the shallow band at an angle of around $\sim 22^\circ$ to the shear plane after straining.

Another example finite strain calculation is shown in Figure 8 for the parameters in Figure 5 (with both slip-surface weakening and grain-reduction and pinning). There is a strong peak in the perturbation amplitude at a shallow angle of $\sim 6^\circ$, rather shallower than the bands seen in experiments.

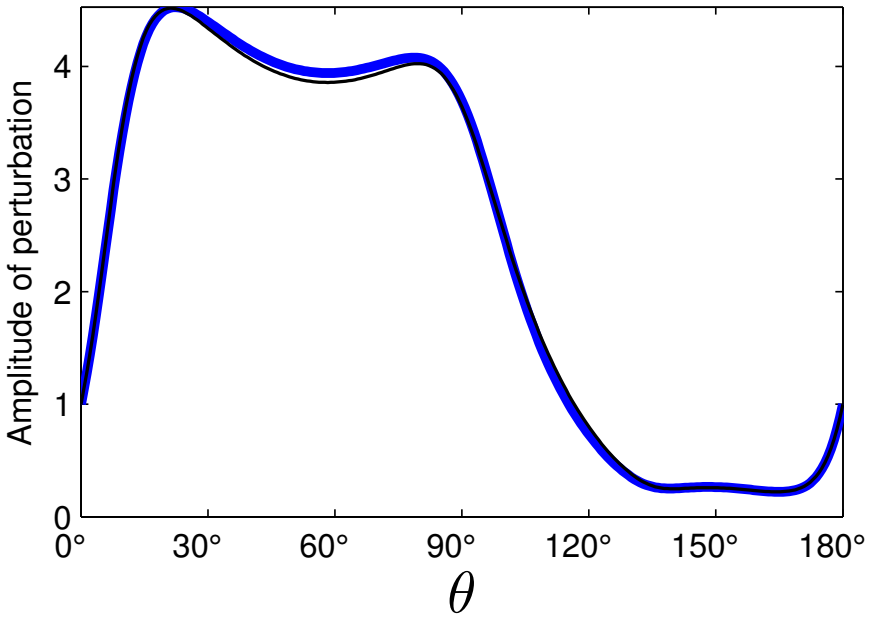

Figure 7. A finite strain calculation for the parameters in Figure 3. Shown is the largest relative amplitude of a perturbation after a total strain $\gamma = 1.0$. Amplitudes greater than 1 represent growth of the perturbation during the straining, amplitudes less than 1 represent decay. The x-axis gives the angle θ of the wave front to the shear plane after straining (at dimensionless time $t = 1$). The thin black line shows the corresponding integration of the asymptotic power-law growth rate given by (54).

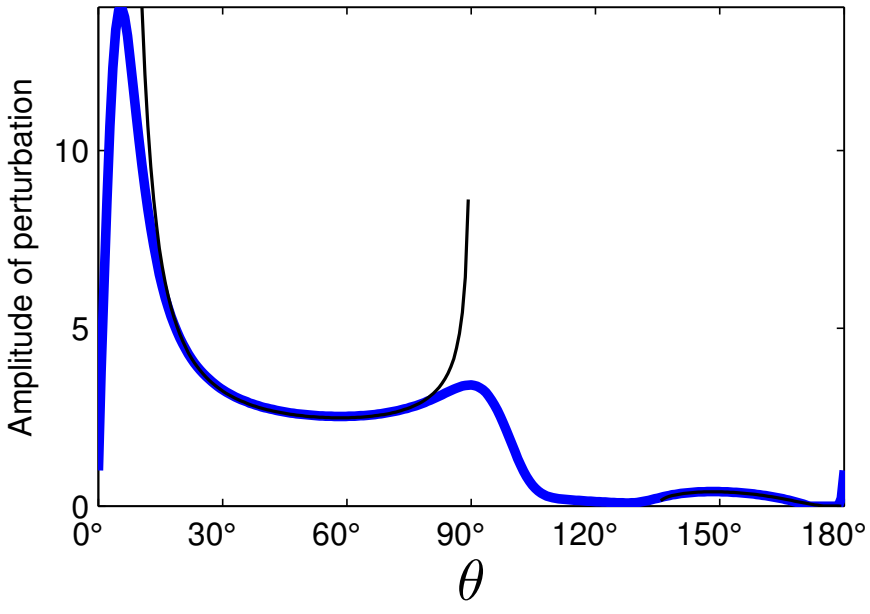

Figure 8. A finite strain calculation as in Figure 7 for the parameters given in Figure 5 to a total strain $\gamma = 1.0$.

6 CONCLUSIONS

We have demonstrated that, in certain reasonable parameter regimes, our model of two-phase damage can produce melt bands that are at a shallow angle to the shear plane, consistent with the experimental observations. These melt bands form in a two-phase medium whose solid grains deform by Newtonian diffusion creep, where the effective non-Newtonian behaviour of the two-phase medium arises from the grain-size (and perhaps also the interface roughness) dependence of the effective shear viscosity. Deformational work acts to increase the interfacial area between the two phases, which retards grain growth by a pinning effect, ultimately leading to a weakening of the two-phase medium. When damage balances healing, and pinning is instantaneous, the two-phase medium behaves as a power-law fluid, and our two-phase damage theory provides some justification for earlier studies of melt band instabilities that have invoked power-law rheologies with large power-law exponents to explain the formation of shallow melt bands (Katz et al. 2006). However, while the presence of a melt phase impedes the grain-growth in the solid (Renner et al. 2002; Faul & Scott 2006), the pinning process is more complex than if the secondary phase were also solid, and, in particular, the effectiveness of pinning depends on various features such as melt interconnectedness, mobility and chemistry (Evans et al. 2001). More theoretical work on grain-growth in partially molten rocks is needed to better quantify this pinning process.

Our models predict that grain-size and interfacial roughness should vary between melt-enriched and melt-depleted regions. Thus a detailed study of grain-size distributions within the experiments could form a useful test of the theory we have presented here. The natural next step for the development of the theory is to perform a full numerical solution of the governing equations, which will allow a detailed description of the time evolution of the bands (Katz et al. 2006; Butler 2012; Katz & Takei 2013; Alisic et al. 2014). With a numerical solution it will be possible to study the connection between the local instantaneous rheology (which we have shown to be effectively strain-rate weakening) and the overall stress-strain curve observed over longer times (which may differ due to the development of the melt bands that concentrate deformation). Further work also needs to be

done to compare the predictions of this two-phase damage theory with those theories based on an anisotropic viscosity tensor, to see which (if any) features in the observations require anisotropy and which can be explained by other means.

Acknowledgements. Support was provided by the National Science Foundation (NSF, grant EAR-1015229), the Natural Environment Research Council (NERC, grant NE/I023929/1), and Trinity College. We thank Stéphane Labrosse, Yasuko Takei, and Sam Butler for their constructive comments that helped improve this manuscript.

REFERENCES

Alisic, L., Rudge, J. F., Katz, R. F., Wells, G. N., & Rhebergen, S., 2014. Compaction around a rigid, circular inclusion in partially molten rock, *J. Geophys. Res.*, **in press**.

Austin, N. & Evans, B., 2007. Paleowattmeters: A scaling relation for dynamically recrystallized grain size, *Geology*, **35**, 343–346.

Bercovici, D. & Ricard, Y., 2003. Energetics of a two-phase model of lithospheric damage, shear localization and plate-boundary formation, *Geophys. J. Intl.*, **152**, 581–596.

Bercovici, D. & Ricard, Y., 2005. Tectonic plate generation and two-phase damage: void growth versus grainsize reduction, *J. Geophys. Res.*, **110**, B03401.

Bercovici, D. & Ricard, Y., 2012. Mechanisms for the generation of plate tectonics by two-phase grain-damage and pinning, *Phys. Earth Planet. Int.*, **202-203**, 27–55.

Bercovici, D. & Ricard, Y., 2013. Generation of plate tectonics with two-phase grain-damage and pinning: Source–sink model and toroidal flow, *Earth Planet Sci. Lett.*, **365**(0), 275 – 288.

Bercovici, D. & Ricard, Y., 2014. Plate tectonics, damage and inheritance, *Nature*, **508**, 513–516.

Bercovici, D., Ricard, Y., & Schubert, G., 2001. A two-phase model of compaction and damage, 1. general theory, *J. Geophys. Res.*, **106**(B5), 8887–8906.

Butler, S. L., 2012. Numerical models of shear-induced melt band formation with anisotropic matrix viscosity, *Phys. Earth Planet Int.*, **200-201**, 28–36.

Craik, A. D. D. & Criminale, W. O., 1986. Evolution of wavelike disturbances in shear flows: a class of exact solutions of the Navier-Stokes equations, *Proc. R. Soc. London Ser. A*, **406**, 13–26.

Daines, M. J. & Kohlstedt, D. L., 1997. Influence of deformation on melt topology in peridotites, *J. Geophys. Res*, **102**, 10257–10271.

Evans, B., Renner, J., & Hirth, G., 2001. A few remarks on the kinetics of static grain growth in rocks, *Int. J. Earth Sciences (Geol. Rundsch.)*, **90**, 88–103.

Faul, U. H. & Scott, D., 2006. Grain growth in partially molten olivine aggregates, *Contrib. Mineral Petrol.*, **151**, 101–111.

Holtzman, B. K., Groebner, N. J., Zimmerman, M. E., Ginsberg, S., & Kohlstedt, D., 2003. Stress-driven melt segregation in partially molten rocks, *Geochem. Geophys. Geosyst.*, **4**, 8607.

Karato, S., 1989. Grain growth kinetics in olivine aggregates, *Tectonophysics*, **168**, 255–273.

Katz, R. F. & Takei, Y., 2013. Consequences of viscous anisotropy in a deforming, two-phase aggregate. part 2. numerical solutions of the full equations, *J. Fluid Mech.*, **734**, 456–485.

Katz, R. F., Spiegelman, M., & Holtzman, B., 2006. The dynamics of melt and shear localization in partially molten aggregates, *Nature*, **442**, 676–679.

King, D. S. H., Zimmerman, M. E., & Kohlstedt, D. L., 2010. Stress-driven melt segregation in partially molten olivine-rich rocks deformed in torsion, *J. Petrol.*, **51**, 21–42.

Kohlstedt, D. L. & Holtzman, B. K., 2009. Shearing melt out of the earth: An experimentalist's perspective on the influence of deformation on melt extraction, *Ann*, **37**, 561–593.

Malvern, L., 1969. *Introduction to the Mechanics of a Continuous Medium*, Prentice-Hall, Englewood Cliff, New Jersey.

McKenzie, D., 1984. The generation and compaction of partially molten rock, *J. Petrol.*, **25**, 713–765.

Qi, C., Zhao, Y.-H., & Kohlstedt, D. L., 2013. An experimental study of pressure shadows in partially molten rocks, *Earth. Planet. Sci. Lett.*, **382**, 77–84.

Renner, J., Evans, B., & Hirth, G., 2002. Grain growth and inclusion formation in partially molten carbonate rocks, *Contrib Mineral Petrol*, **142**, 501–514.

Ricard, Y. & Bercovici, D., 2009. A continuum theory of grain size evolution and damage, *J. Geophys. Res.*, **114**, B01204.

Rozel, A., Ricard, Y., & Bercovici, D., 2011. A thermodynamically self-consistent damage equation for grain size evolution during dynamic recrystallization, *Geophys. J. Int.*, **184**(2), 719–728.

Smith, C. S., 1948. Grains, phases, and interfaces: An interpretation of microstructure, *Trans. A.I.M.E.*, **175**, 15–51.

Spiegelman, M., 2003. Linear analysis of melt band formation by simple shear, *Geochem. Geophys. Geosyst.*, **4**, 8615.

Stevenson, D. J., 1989. Spontaneous small-scale melt segregation in partial melts undergoing deformation, *Geophys. Res. Lett.*, **16**, 1067–1070.

Takei, Y. & Holtzman, B., 2009. Viscous constitutive relations of solid-liquid composites in terms of grain boundary contiguity: 3. Causes and consequences of viscous anisotropy, *J. Geophys, Res.*, **114**, B06207.

Takei, Y. & Katz, R. F., 2013. Consequences of viscous anisotropy in a deforming, two-phase aggregate. part 1. governing equations and linearized analysis, *J. Fluid Mech.*, **734**, 424–455.